A laser-induced wide-range thin-film temperature sensor without additional anti-oxidative encapsulations

OPEN ACCESS
IMMT | IOP Publishing
International Journal of Extreme Manufacturing
Int. J. Extrem. Manuf. **7** (2025) 065508 (13pp)
https://doi.org/10.1088/2631-7990/adefa2

A laser-induced wide-range thin-film temperature sensor without additional anti-oxidative encapsulations

Yuyu Hou, Haibo Xie*, Yibo Li, Zimo Cai, Bin Zhang, Yang Ju, Huayong Yang and Kaichen Xu*

State Key Laboratory of Fluid Power and Mechatronic Systems, School of Mechanical Engineering, Zhejiang University, Hangzhou 310027, People's Republic of China

E-mail: hbxie@zju.edu.cn and xukc@zju.edu.cn

Received 1 April 2025, revised 8 May 2025
Accepted for publication 14 July 2025
Published 29 July 2025

Abstract

Extreme environments challenge the structural health monitoring of advanced equipment. In-situ dynamic tracking temperature is of particular value due to its enormous impact on material properties. However, the realization of such integrated temperature sensors typically requires complicated layer-by-layer molding and sintering processes including additional thermal barrier coatings. Herein, we report a laser-induced in-situ conductive passivation strategy for the fabrication of a thin-film based wide-range temperature sensor. The instantaneous thermal effect of laser irradiation creates crystalline conductive traces in response to temperature variations. Synchronously, it also allows the formation of an amorphous antioxidative layer without necessitating extra protective coatings. Such configuration enables precise real-time sensing across −50 °C to 950 °C following the Steinhart-Hart equation. It also exhibits durable performance with only 1.2% drift over 20 hours during long-term high-temperature, instant thermal shock, frequent wearing, and severe vibration. This in-situ, facile laser manufacturing strategy holds great promise in structural health monitoring and fault diagnosis for advanced equipment working in extreme environments.

Supplementary material for this article is available online

Keywords: extreme environments, in-situ integration, temperature sensors, laser sintering, laser-induced passivation

* Authors to whom any correspondence should be addressed.

1. Introduction

Extreme environments, such as ultra-high pressure, harsh corrosion, violent vibration, and superhigh or ultra-low temperature, are long-standing and critical challenges for ensuring fault-free operation of advanced equipment[1–3]. Capture of physical information from components themselves or ambience, such as temperature, pressure, vibration, thermal shocks, and strain, is crucial for dynamic failure detection[4–6]. Particularly, temperature monitoring is extensively studied, especially in high-temperature scenarios, due to its substantial impact on material properties[7–9]. Typically, temperature sensors are integrated with components of interest through the conformal attachment of flexible thermal-sensitive films, embedment of rigid sensors, or in-situ fabrication[10–12]. However, flexible thin-film-based sensors generally suffer from decomposing polymer substrates at relatively high temperatures (generally <500 °C)[13–15]. Additionally, the sensor embedding process may compromise the mechanical strength of precision components[16,17].

The strategy of in-situ integrated sensors can circumvent the aforementioned issues by virtue of their seamless conformability and being free from thin polymers[18–20]. Such thin-film-based temperature sensors made from polymer-derived ceramics or precious metal platinum have demonstrated temperature sensing exceeding 1 000 °C. Realization of these sensors typically involves layer-by-layer molding and sintering processes[21–23]. This allows the formation of a temperature-sensitive layer, a thermal stress-matching layer, and a thermal barrier coating[24–26]. Particularly, the thermal barrier coating is crucial as a protective layer against the oxidation (e.g., superalloys and ceramics) or decomposition (e.g., indium tin oxide and ruthenium oxide) of sensitive layers[27–31]. Films without such thermal barrier encapsulation typically cannot withstand temperatures above 800 °C, because they cannot spontaneously form a dense anti-oxidation layer like bulk materials. However, fabrication of these multilayers generally requires multiple manufacturing techniques, such as sputtering deposition, chemical/physical vapor deposition, or printing[32–36]. Furthermore, preparation of each layer may suffer from high-temperature sintering for tens of hours in an inert gas[37–39].

In this article, we report a thin-film based wide-range temperature sensor via a laser-induced in-situ conductive passivation strategy. This requires no additional anti-oxidative encapsulations and thermal stress matching layer, substantially circumventing the tedious fabrication processes. During the laser treatment, the precursor nanoparticles fuse and aggregate to create homogeneous and continuous titanium diboride (TiB_2) conductive traces inside the film. Synchronously, a silicon oxide/boron oxide (SiO_2-B_2O_3) anti-oxidative protective layer is formed on the exterior surface to safeguard the conductive traces. The sensing curve of the proposed film-based temperature sensor exhibits a strong correlation with the Steinhart-Hart equation across a wide detection range of −50 °C to 950 °C. Furthermore, the exceptional stability with less than 1% drift is observed in durable cycle tests and a superior response time of 5.5 seconds is demonstrated. The proposed facile yet reliable manufacturing of passivated thermal-sensitive double layers demonstrates the potential towards wide-range temperature monitoring.

2. Results and discussion

2.1. Laser-induced in-situ conductive passivation for wide-range temperature sensors

The proposed in-situ conductive passivation strategy constructs a high-temperature resistant ceramic-based film via continuous-wave (CW) green laser direct writing. This method instantaneously transforms electrically insulating titanium diboride (TiB_2)/silicon carbide (SiC) ceramic inks into a double-layer conductive film of TiB_2/SiO_2-B_2O_3 (i.e. crystalline conductive layer and amorphous antioxidative layer) through physical and chemical processes, offering superior tolerance to harsh environments (Figure 1(a-i)). In contrast to the aforementioned strategy, the conventional ceramic sintering techniques have limitations in energy efficiency, complicated processes, and atmosphere conditions. Furthermore, such inorganic ink tends to gradually oxidize rather than form dense ceramic during the long-term thermal sintering process (Figure 1(a-ii)). To address this issue, the proposed method utilizes laser direct writing by virtue of its instantaneous heat effect and can take place even in an ambient atmosphere. The film, fabricated by the laser, is dense, uniformly conductive, and temperature-sensitive across a wide range of −50 °C to 950 °C (Figure 1(a-iii)), offering a promising approach for extreme temperature monitoring in numerous fields, such as battery management system, aerospace, semiconductors, and natural gas industry.

To be specific, the interaction between laser and the matter is primarily manifested in two aspects: laser sintering and laser-induced passivation. Laser sintering is a morphological change process, forming crystalline TiB_2 conductive traces (Figure 1(b)). During this process, TiB_2 and SiC particles, serving as photothermal converters, absorb most of the laser energy and convert it into heat. This process rapidly increases their temperature to the melting point and leads to the decomposition of organic components in the precursor, such as solvents and dispersing agents. The molten particles form neck connections and agglomerate into the larger grains until a uniform and continuous conductive trace is produced. Electrons migrate freely within the dense ceramic in a laser-treated film whereas their movement is hindered by the interstices between particles in an initial film (insets in Figure 1(b)).

Simultaneously, laser-induced passivation, a chemical-induced change process that primarily affects the film's surface, generates amorphous anti-oxidation protective phases (Figure 1(c)). Due to the thermal effect of laser, boron (B) and silicon (Si) atoms promptly attain the essential activation energy (E_a) for the oxidation reaction, rapidly producing boron oxide (B_2O_3) and silicon oxide (SiO_2) as follows,

$$2TiB_2 + 5O_2 \xrightarrow{laser} 2TiO_2 + 2B_2O_3 \quad (1)$$

$$SiC + 2O_2 \xrightarrow{laser} SiO_2 + CO_2 \uparrow \quad (2)$$

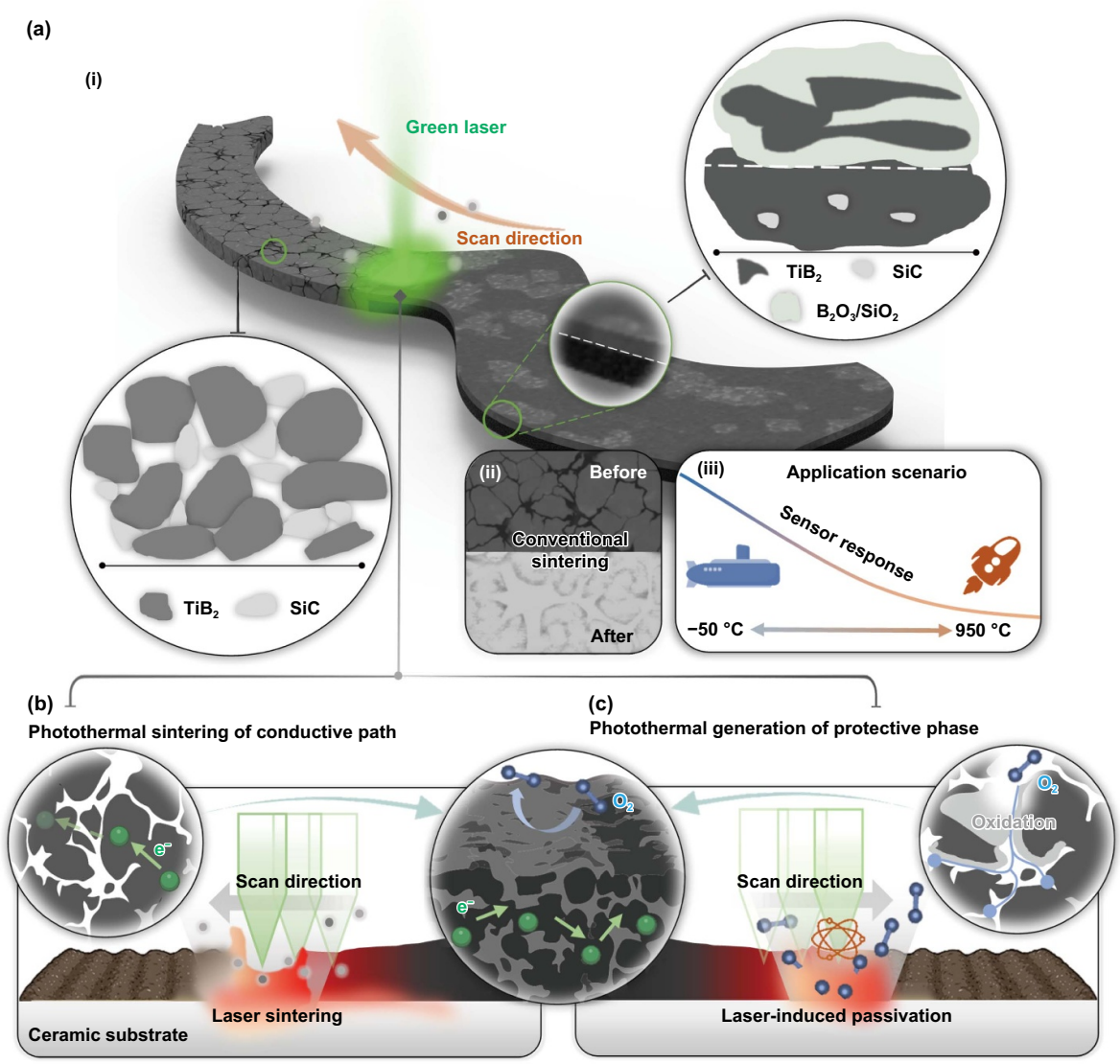

Figure 1. Conceptual illustration of a laser-induced temperature-tolerant film without additional anti-oxidative encapsulations for sensing in extreme environments. (a) Schematic of the proposed laser-induced double-layer films compared to the conventional thermal sintering. (a-i) Schematic of the material and morphology of the film before and after laser direct writing. (a-ii) Schematic of the oxidized film caused by conventional thermal sintering. (a-iii) Schematic of the wide detection range of temperature for the proposed film-based temperature sensor. (b) Schematic of the formation process of continuous and uniform TiB_2 conductive traces using laser-induced sintering. The left and center insets denote the ease of electron migration before and after laser processing, respectively. (c) Schematic of the production of an anti-oxidative glassy protective phase during laser-induced passivation. The right and center insets denote the difference in the ease of oxygen penetration before and after laser processing, respectively.

Subsequently, B, Si, and O atoms form covalent bonds within the instantaneous ultra-high temperature field induced by the laser. This reaction culminates in the formation of amorphous SiO_2-B_2O_3 glassy phase material during the following rapid cooling process after laser writing[40–42],

$$B_2O_3 + SiO_2 \xrightarrow{laser} binary\ SiO_2 \cdot B_2O_3 \tag{3}$$

This amorphous glassy phase material is endowed with the exceptional ability to hinder oxygen penetration, thereby safeguarding the conductive traces against oxidative degradation across an extensive temperature range[43]. In contrast, in the pristine film, nanoparticles are bounded by organic matter. The volatilization of the organic constituents and B_2O_3 using conventional thermal annealing leads to the formation of porous microstructures. It inhibits the formation of an effective oxide barrier (insets in Figure 1(c)).

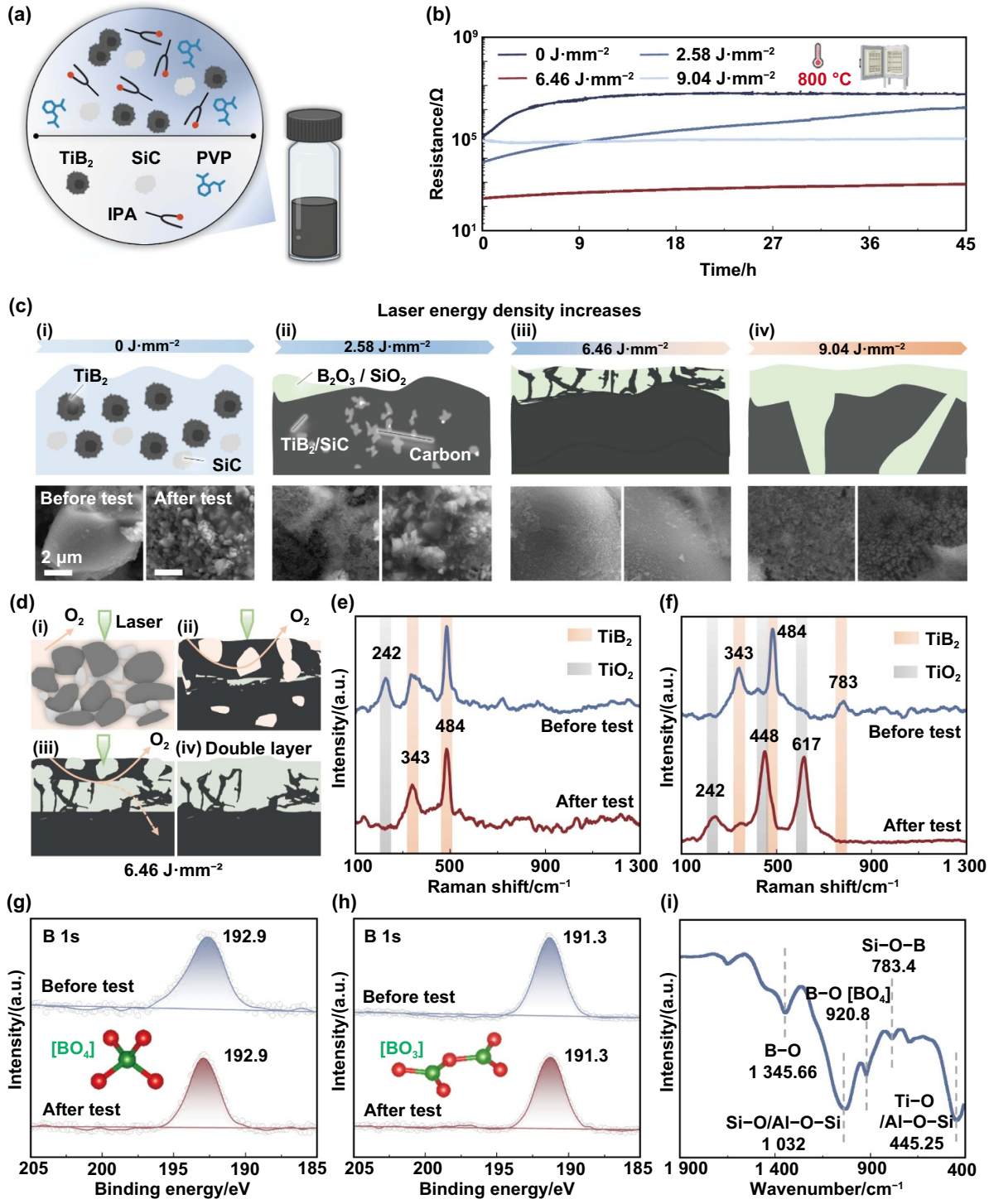

Figure 2. Mechanisms and characterizations of high-temperature resistant films. (a) Schematic of the functional TiB_2/SiC ink composition. (b) High-temperature durability tests of films prepared with different laser energy densities. (c) Schematics of the material morphology in different films as the laser energy density increases. (d) Schematics of the time evolution of a film during a 6.46 J·mm^{-2}-laser direct writing. Raman spectra of (e) the F-6.46 sample and (f) the F-0 sample before and after the high-temperature test, respectively. XPS spectra of B 1s for (g) the F-6.46 sample and (h) the F-0 sample, both before and after the high-temperature test, respectively. (i) FT-IR spectra of the F-6.46 sample after test.

The precursor ink mainly comprises TiB_2 particles, SiC particles, isopropyl alcohol (IPA), and polyvinylpyrrolidone (PVP) (Figure 2(a)). Among them, PVP, serving as a dispersant, plays a pivotal role in preventing the aggregation of TiB_2 and SiC particles, ensuring their uniform dispersion. Due to its volatility, IPA is chosen as a solvent to expedite the transition process from ink to film. Given the critical roles of TiB_2 and SiC particles as primary backbones of the

precursor film, it is essential to rationally regulate their mixture ratios.

A series of inks were prepared with varying TiB_2:SiC mass ratios of 10:0, 10:1, 10:2, 10:4, and 10:6, respectively (Figure S1). After spin-coating films using the aforementioned inks, 75 samples were obtained via laser direct writing with 15 different energy densities, evenly distributed within the range of 0−7.5 J·mm^{-2}. By evaluating the sheet resistance of these samples before and after the high-temperature test (800 °C, 3 hours), their electrical conductivity and oxidation conditions were analyzed. It is found that only the film with a mass ratio of 10:2 subjected to an appropriate laser energy density, demonstrates consistent and stable conductivity at elevated temperatures, thereby highlighting its superior high-temperature tolerance (Figure S2). Insufficient SiC compromises the formation of continuous SiO_2-B_2O_3 protective phases, critically degrading the composite's high-temperature oxidation resistance. It also necessitates elevated laser power input during sintering due to the relatively small absorption coefficient of TiB_2 ($\alpha = 2.1 \times 10^4$ cm^{-1} at 532 nm) compared to that of SiC ($\alpha = 7.8 \times 10^4$ cm^{-1})[44,45]. However, an excess of SiC content may obstruct conductive trace pathways, probably leading to insulation.

2.2. Influence of laser fluence on in-situ conductive passivation in the films

Employing the optimized ratio of ink, a high-temperature resistant film was fabricated through laser treatment with an energy density of 6.46 J·mm^{-2} (F-6.46), a scanning speed of 20 mm·s^{-1}, and a hatch spacing of 20 μm. It is worth mentioning that the average thickness of the films is less than 5 μm (Figure S3). The heat loss of laser in the vertical direction is almost negligible. Thermal field simulations indicate that the temperatures at the bottom and top of the film under laser irradiation are nearly identical (Figure S4). To demonstrate the remarkable oxidation resistance of the F-6.46 sample at high-temperature conditions, the durability test was conducted at 800 °C for a prolonged period of 45 hours. To further clarify the aforementioned role of laser writing, three comparative tests were performed with laser energy densities of 0 J·mm^{-2} (F-0), 2.58 J·mm^{-2} (F-2.58), and 9.04 J·mm^{-2} (F-9.04), respectively. Among them, the F-6.46 sample demonstrated feasible electrical conductivity and superior high-temperature oxidation resistance (Figure 2(b)). In contrast, the F-0 and F-2.58 samples oxidized rapidly and finally failed at such an elevated temperature. Additionally, the F-9.04 sample demonstrated exceptionally low electrical conductivity with room-temperature electrical resistance surpassing 10^9 Ω, which approached the insulating characteristics of structural ceramics employed in high-temperature applications. Such extremely high electrical resistivity hinders its applications in sensing systems despite its temperature-invariant electrical behavior during the durability test.

In the initial precursor film without laser treatment (F-0), the TiB_2 and SiC particles are loosely stacked, with diverse gaps that restrict the electron movement (Figure 2(c-i)). During conventional thermal sintering (ambient atmosphere) (Figure S5(a)), the F-0 sample forms partially conductive traces. However, the traces are susceptible to ongoing oxidation due to the absence of protective layer to impede oxygen penetration. Scanning electron microscope (SEM) images demonstrate that tiny oxidative particles are produced subjected to the high temperature. By applying a restively small energy density (F-2.58), the surfaces become rough owing to the growth and fusion of TiO_2 crystals at an elevated temperature (Figure 2(c-ii)). The oxidation-mediated morphological evolution demonstrates a correlation with the gradual rise in electrical resistance (Figure S5(b)). Laser sintering enhances the connections and promotes the densification of TiB_2, while simultaneously breaking the covalent bonds of carbon, leading to the formation of amorphous carbon (Figure 2(c-ii)). Therefore, the F-2.58 sample possesses the optimal conductivity before the durability test. Nevertheless, the temperature of materials induced by this laser fluence is insufficient to reach the reaction rate for the aforementioned laser-induced passivation (Note S1). As a result, the generated SiO_2-B_2O_3 is inadequate to fully encapsulate the conductive traces, rendering the F-2.58 sample susceptible to oxidation at elevated temperatures, similar to the F-0 sample (Figures 2(c-ii) and S5(c)).

As the laser energy density further increases, the F-6.46 sample maintains continuous conductive traces and forms adequate anti-oxidative phases in the surface layer (Figures 2(c-iii) and S5(d)). It exhibits almost no surface change as observed in SEM images, which is attributed to the formation of SiO_2-B_2O_3 protective phases. In contrast, continuously increasing the laser energy density enables trigger excessively rapid laser-induced passivation reaction. Such reaction not only consumes TiB_2 but also generates redundant SiO_2-B_2O_3 composites, thereby disrupting the conductive trace networks (Figure 2(c-iv)). Tiny cracks are found in the SEM image of the F-9.04 sample, probably due to the excessive reaction of laser-induced passivation. As a result, this sample shows almost insulating properties (Figure S5(e)).

By comparing their optical images, the four films via different laser energy densities exhibited evident discrepancies (Figure S6). Notably, the colors of the F-0 and F-2.58 samples changed significantly from black to white after the durable high-temperature test, indicating severe oxidation. However, this phenomenon was not observed in the F-6.46 and F-9.04 samples, whereas F-9.04 had already suffered from partial detrimental oxidation due to the excessive laser irradiation. Further detailed surface morphologies are displayed in Figure S7.

In the process of the laser treatment with an energy density of 6.46 J·mm^{-2}, the precursor nanoparticles undergo sequential phase transformations (Figure 2(d)). First, organic matters in the film decompose thermally, generating gaseous byproducts, and the initial coalescence of nanoparticles forms a densified conductive matrix. Simultaneously, partial nanoparticles react with oxygen to produce the SiO_2-B_2O_3 composite. Second, this process keeps going until all the organic matters decompose. The pores created by the

decomposition in the subsurface layer are filled by the melt and aggregation of nanoparticles, and the surface oxidation produces interfacial passivating substances. These passivating substances form a diffusion barrier that effectively prevents oxygen from permeating into the subsurface. Third, the oxide layer grows thicker and extends toward the surface. After laser scanning, the film rapidly cools, and the metastable oxides form a stable amorphous oxide protective layer.

2.3. Characterizations of in-situ passivated high-temperature resistant conductive films

To substantiate the formation mechanisms and antioxidative capacity of the high-temperature resistant film, characterizations of Raman spectra, X-ray diffraction (XRD), Fourier transform infrared (FT-IR), X-ray photoelectron spectroscopy (XPS), energy dispersive spectrometer (EDS), and transmission electron microscopy (TEM) were performed, respectively. First, Raman spectra results, before and after the durable high-temperature test, distinctly reveal the oxidation status of the films. The film generated by the optimized laser energy density (i.e. F-6.46), exhibits prominent characteristic peaks of TiB_2 centered at 343 cm^{-1} (corresponding to the symmetric stretching vibration of the B–Ti–B bond) and 484 cm^{-1} (corresponding to the bending vibration of the Ti-B bond) both before and after test, respectively (Figure 2(e))[46]. This demonstrates its exceptional oxidation resistance, even after exposure to 800 °C. A minor peak (242 cm^{-1}) of titanium oxide (TiO_2) is also observed, probably indicating the byproduct of SiO_2-B_2O_3 reaction (Note S1). In contrast, the Raman spectra of samples without laser processing (i.e. F-0) imply severe oxidation under high-temperature conditions (Figure 2(f)). Initially, peaks centered at 343 cm^{-1}, 484 cm^{-1}, and 783 cm^{-1} confirm the existence of TiB_2 as the film's primary constituent. However, these peaks disappear after the 3 hour test at 800 °C. The Raman peaks completely shift to the characteristic peaks of TiO_2 (i.e. 242 cm^{-1}, 448 cm^{-1}, and 617 cm^{-1}), suggesting that TiB_2 is oxidized to TiO_2. Among them, a broad composite vibration peak caused by the polyphonon scattering process is clearly observed at 242 cm^{-1}. The peak at 448 cm^{-1} corresponds to the symmetric bending mode of Ti–O–Ti, and the peak at 617 cm^{-1} corresponds to the stretching vibration of Ti–O–Ti[47]. It indicates that such untreated film is extremely prone to oxidation at high temperatures. It also implies that the conventional sintering treatment easily leads to oxidation-induced failure in the film.

In addition, insufficient or excessive laser energy density also results in film failure. For instance, the Raman spectra of the F-2.58 sample verify the same oxidation behavior as F-0 and the formation of carbon (i.e. D and G peaks) (Figure S8(a)). Although Raman spectra of the F-9.04 sample exhibit the desired stability, it has already suffered from severe oxidation caused by the higher laser power. This is confirmed by the Raman results obtained before the durability test. It reflects obvious peaks of TiO_2 and a more pronounced amorphous feature as implied by the enhanced Raman intensity within the 1 000−1 700 cm^{-1} range (Figure S8(b))[48]. In addition, XRD results exhibit consistent material changes as Raman characterizations (Figure S9). Only the F-6.46 demonstrates obvious characteristic peaks of TiB_2 both before and after the test, confirming its antioxidant ability (Figure S9(c)). The unmarked impurity peaks in Figure S9 are all characteristic peaks of the α-Al_2O_3 substrate.

It is noteworthy that the outstanding anti-oxidation ability is attributed to the amorphous glass phase of SiO_2-B_2O_3, rather than SiO_2 or B_2O_3 alone. The binding energy of B 1s (192.9 eV) shown in high-resolution XPS spectra indicates that a B atom is coordinated with four O atoms in the F-6.46 sample (Figure 2(g)). The presence of [BO_4] reveals that boron exists in the form of borates (i.e. SiO_2-B_2O_3). The Si 2p peak (Si-O: 102.5−103.5 eV) and O 1s peak (silicates: 531.5−532.5 eV) observed in the XPS results also substantiate the formation of SiO_2-B_2O_3 phase in the F-6.46 sample (Figure S10). In contrast, a film without SiC doping fabricated via the same laser parameter shows that a B atom is coordinated with three O atoms (191.3 eV) (Figure 2(h)). The presence of [BO_3] indicates that boron exists in the form of B_2O_3. Furthermore, the O 1s peak shifts from 533 eV (before durability test, B_2O_3) to 531.4 eV (after test, TiO_2) of the control group, implying that B_2O_3 lacks efficient antioxidative capacity and the film suffers from severe oxidation at high temperatures (Figure S11). In addition, the FT-IR spectra (Figure 2(i)) display the predominant chemical bonds in the F-6.46 sample, including Ti–O (445.25 cm^{-1}), Si–O–B (783.4 cm^{-1}), B–O [BO_4] (920.8 cm^{-1}), Si–O (1 032 cm^{-1}) and B–O (1 345.66 cm^{-1}), respectively. The presence of Si–O–B and B–O [BO_4] peaks also verifies the distribution of the binary SiO_2-B_2O_3 glass phase in the F-6.46 sample.

Additionally, the glassy SiO_2-B_2O_3 serves as a desired adhesive and may form chemical bonds with the Al_2O_3 substrate, leading to superior adhesion between the film and substrate. The peaks at 445.25 cm^{-1} and 1 032 cm^{-1} observed in the FTIR spectrum are likely characteristics of Al–O–Si bonds (Figure 2(i)). To further probe into the chemical bonding at the interface, comparative XPS characterizations were performed (Figure S12). The Al 2p peak of the original Al_2O_3 substrate is observed at 74.3 eV, whereas at the interface of F-6.46 and Al_2O_3 substrate, it shifts to 73.82 eV. This shift indicates a change in the bonding environment of Al atoms, suggesting that chemical bonding, such as Al–O–Si and Al–O–B, may exist at the interface.

To further clarify the distribution of SiO_2-B_2O_3 and TiB_2, TEM was performed to reveal the structures of film processed by the optimized laser energy density (i.e. 6.46 $J{\cdot}mm^{-2}$), which was mainly composed of two layers (Figure 3(a)). The amorphous SiO_2-B_2O_3 encompassing polycrystalline TiB_2 makes up the external antioxidative layer (Figure 3(b)). Additional fast Fourier transform (FFT) is performed on areas A and B of Figure 3(b), respectively. As can be observed, area A exhibits clear amorphous phase properties, whereas area B displays polycrystalline properties (Figure 3(c)). Amorphous SiO_2-B_2O_3 features the anti-oxidant by isolating oxygen, while polycrystalline TiB_2 connects in parallel with the interior conduction layer, ensuring that the whole film exhibits a conductive state (Figure S13).

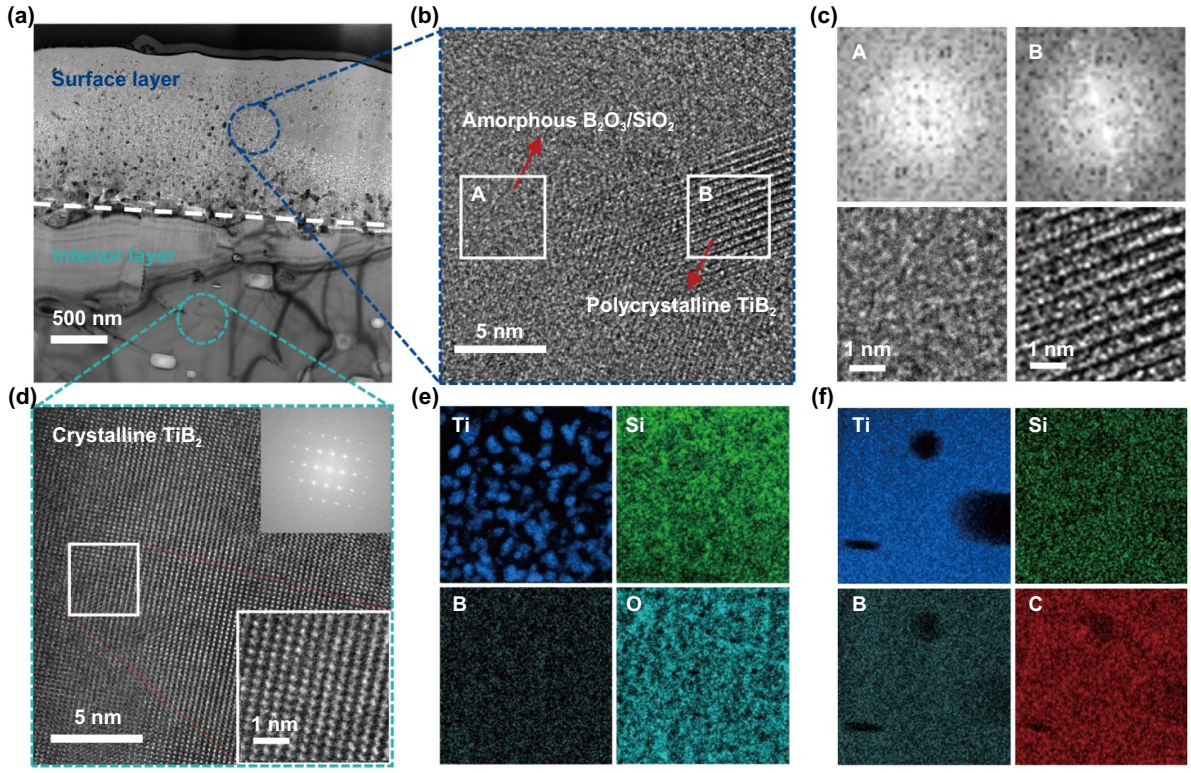

Figure 3. TEM and EDS analysis of high-temperature resistant films. (a) Cross-section TEM image of the film fabricated by the laser energy density of 6.46 J·mm^{-2}. (b) TEM image of the surface layer. The area A represents an amorphous phase and area B represents a polycrystalline phase. (c) Enlarged TEM and FFT images of areas A and B, respectively. (d) TEM image of interior layer. The insets denote enlarged TEM and FFT of the white-framed area, respectively. (e) EDS element (Ti, Si, B, and O) distribution map of the surface layer. (f) EDS element (Ti, Si, B, and C) distribution map of the interior layer.

Crystalline TiB_2 features can be found in the interior conduction layer (Figure 3(d)). The external layer's wrapped state is further confirmed by the EDS analysis of the two layers. The titanium (Ti) elements in the exterior layer are dispersed in a scattered manner (Figure 3(e)), while whole elements in the interior layer are distributed uniformly (Figure 3(f)). Additionally, according to the EDS with a full cross-section, the element content of the two layers differs significantly (Figure S14). It is remarkable to recognize that the precursor film, fabricated by conventional sintering, is prone to oxidation failure without the formation of SiO_2-B_2O_3 during processing. Compared with laser writing, this phenomenon is probably attributed to two reasons. First, the B_2O_3 (melting point: 450 °C) volatilizes during the prolonged sintering process, preventing the formation of the binary SiO_2-B_2O_3 phase. This issue can be suppressed by the instantaneous nature of laser treatment. Second, even if a sufficient amount of B_2O_3 remains, crystalline SiO_2-B_2O_3 may form instead of glassy SiO_2-B_2O_3 during the slow cooling annealing process (Figure S15). The critical cooling rate (R_c) is pivotal in the formation of glassy SiO_2-B_2O_3. When the cooling rate exceeds this threshold, atoms in the melt lack sufficient time for long-range diffusion or rearrangement into an ordered lattice structure, resulting in an amorphous state, i.e., glassy SiO_2-B_2O_3. The R_c can be calculated by $R_c = (T_m - T_g)/\tau$, where T_m is the melting point of the mixture (i.e., SiO_2 and B_2O_3), T_g is the glass transition temperature, and τ is the structural relaxation time[49,50]. A cooling rate exceeding 200 °C·min^{-1} is essential, which is challenging to achieve in conventional sintering but attainable with laser treatment.

2.4. Characterizations of the in-situ passivated wide-range temperature sensors

Due to the remarkable temperature tolerance in harsh environments, the composite film treated by laser is employed as the active components for temperature sensors operating across −50 °C to 950 °C. The overall structure of the sensor is shown in Figure S16. The principle of temperature detection is thermal resistance, which is the simplest and most widely detection mechanism in high-temperature sensing. As the temperature rises, more electrons in the film are excited from the valence band to the conduction band, thereby increasing the carrier concentration and reducing the resistance. As can be seen, multiple temperature sensor samples all maintain superior stability and repeatability throughout over 30 hours of 100−800 °C cycle tests (Figure 4(a)). The heating and cooling hysteresis curves for six consecutive cycles further illustrate the robustness of the sensor in tracking temperature (Figure 4(b)). The maximum measurable value of the sensor for short-term temperature detection is demonstrated to be 950 °C, through the curves across 100−950 °C, showing an 8.1% resistance drift (1.2% drift in temperature) after 3 cycles (>20 hours) (Figure S17). The divergence observed

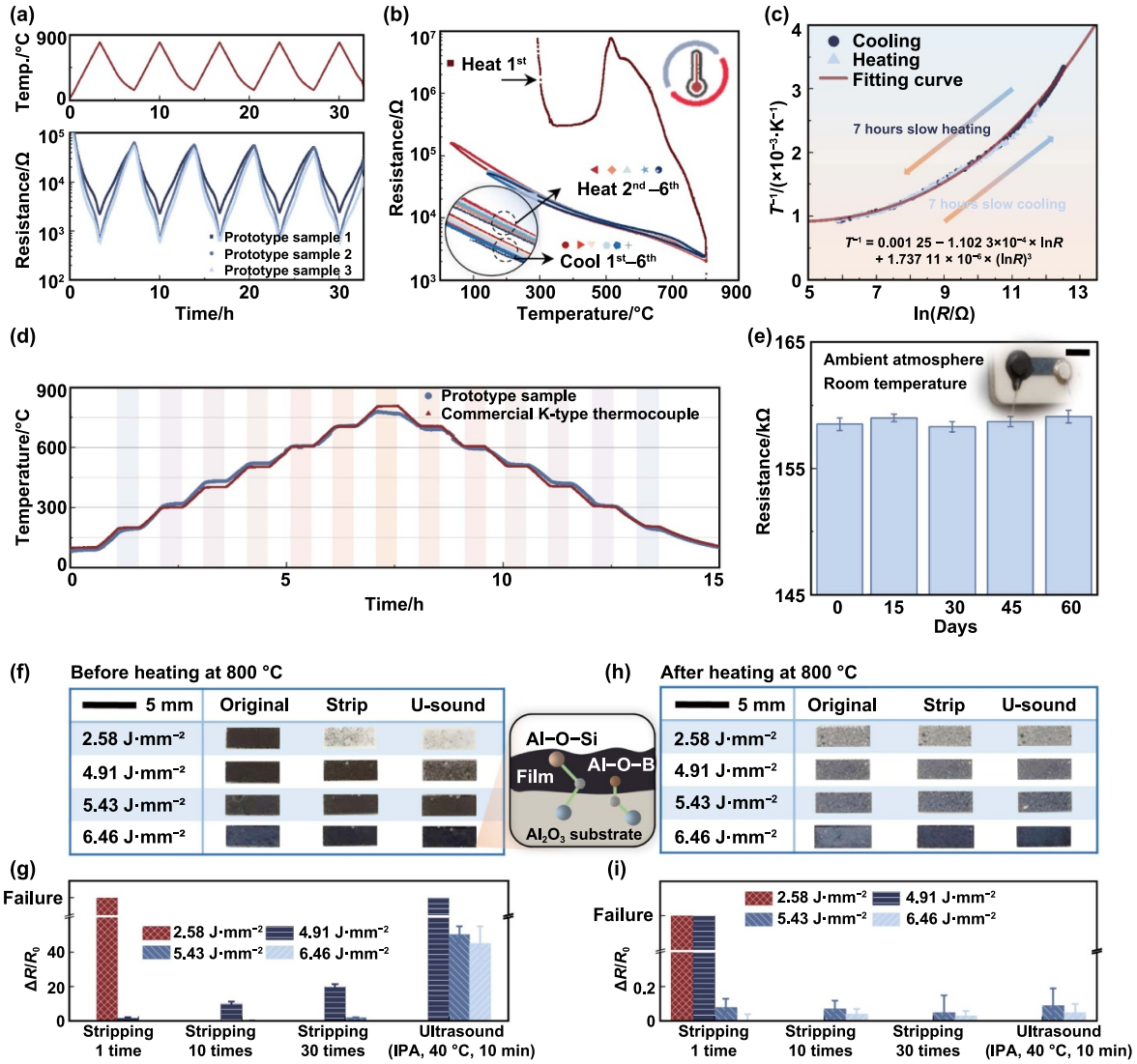

Figure 4. Characterizations of film-based temperature sensor and adhesion test. (a) Long-time cyclic measurements of the prototype samples under temperature variation from 50 °C to 800 °C. (b) The hysteresis curve of the sensor, with an inset showing the magnified view. (c) The 7-hour heating curve and the cooling curve, along with their fits to the Steinhart-Hart formula and the corresponding fitting equations. (d) The time-dependent resistance changes ratio of the proposed temperature sensor by varying the chamber temperature from 100 °C to 800 °C, compared with a commercial K-type thermocouple. (e) Resistance changes of the sensor after being stored in ambient conditions at room temperature for 60 days. The inset shows a photograph of the sensor. Optical images of the four types of films (F-0, F-2.58, F-6.46, and F-9.04), (f) before and (h) after heating at 800 °C, in their original state, after 30 cycles of 3 M tape stripping tests, and after the ultrasonic destruction test, respectively. The inset schematic illustrates the interface bonding. Resistivity changes of the four types of films, (g) before and (i) after heating at 800 °C, after the tape stripping test, and the ultrasonic destruction test, respectively.

in the first heating process is probably attributed to the reduction of the film's pores, which are mainly generated by the laser-induced CO_2 gas release and may be filled by the glassy SiO_2-B_2O_3 (Figure 4(b)). The first cycle of thermal treatment further condenses the films, enabling the steady electrical performance in the following cycles. During a 7 hour heating and cooling cycle across 100−800 °C, the hysteresis curves almost overlap with a deviation of less than 1%, indicating an almost neglectable hysteresis effect (Figure 4(c)). Furthermore, these data are the calibration points of the sensor. The curve is accurately fitted by a Steinhart-Hart equation because it is highly suitable for ceramic semiconductor materials and negative temperature-sensitive thermal resistance[51], with $R^2 = 0.989\,5$, as follows,

$$1/T = 0.00125 - 1.1023 \times 10^{-4} \ln R + 1.73711 \times 10^{-6} (\ln R)^3 \quad (4)$$

where T is the temperature, and R is the resistance of sensor. The temperature-sensitive curves of the batch samples are shown in Figure S18. Compared with a commercial K-type thermocouple, the sensor exhibits remarkable steadiness in both low and high-temperature environments (Figure 4(d)). Due to the absence of encapsulation requirements, the thin-film sensor also exhibits outstanding response speed. When transferred from room temperature to an oven at 150 °C, it shows a response time of 5.5 seconds (Figure S19). Aging performance is also an important index for sensors. The almost negligible variation of resistance of the sensor after being stored in an ambient environment for up to 60 days is indicative of its commercial potential (Figure 4(e)). It also indicates that the resistance tolerance of the sensor is less than 1%. In addition, the comparative tests are carried out with only Al_2O_3 substrate, original ink, and Ag/Pd solder joints, to confirm that the observed temperature-sensitive characteristics originate from the proposed film (Figure S20). The former two samples are considered as insulators ($>10^5$ Ω at 800 °C), whereas the latter shows thousands of times lower resistance compared to the sensitive film. The response of film to strain is also characterized (Figure S21). Under a maximum strain input of 0.05%, the sensor exhibits a maximum resistance change of 0.65%. Compared with the resistance changes caused by temperature, the effect of strain is almost negligible. Additionally, a comprehensive comparison is made between the proposed thin-film temperature sensor and the prior arts reported in recent research in terms of manufacturing methods, sintering time, materials, long-term monitoring range, stability, etc. (Table S1). The proposed sensor has significant advantages in terms of manufacturing convenience, cost, and stability.

Additionally, the film demonstrates superior adhesion to the substrate surface. Tape stripping and ultrasonic destruction tests are carried out to demonstrate the adhesion property. Figure S22 illustrates the films undergoing 30 cycles of 90°-vertical tape stripping test, followed by ultrasonic treatment in IPA at 40 °C for 10 minutes. Optical images (Figure 4(f)) and resistance changes (Figure 4(g)) apparently manifest that adhesion is enhanced with elevated laser energy density, owing to the enhanced chemical bonding (inset in Figure 4(f)) by intensified thermal effect. Moreover, the adhesion is further enhanced through high-temperature treatment, as demonstrated by the negligible variation in electrical properties even after the ultrasonic destruction test (Figures 4(h) and (i)). It is probably because of the prolonged thermal effect forming more chemical bonds at the film-substrate interface than the effect induced by the laser alone. A control experiment without SiC doping shows the electrical failure of the film after ultrasonic treatment, implying the protective role of the amorphous glassy SiO_2-B_2O_3 (Figure S23). Therefore, the superior adhesion is probably attributed to two principles. On the one hand, the thermal effect of laser facilitates the formation of chemical bonds among Si, Ti, and B atoms in the film and O atoms in the substrate. On the other hand, the glassy SiO_2-B_2O_3 encapsulates conductive traces as binders.

As a proof of concept, the proposed laser direct writing of ceramic is employed for the in-situ fabrication of a temperature sensor on a silicon nitride bearing (Figure 5(a)). This type of bearing is widely applied in high-temperature components which operate at temperatures exceeding 600 °C, including aero-engines, gas turbines, and metallurgical high-temperature rolling mills. Traditional sensing methods, such as armored thermocouples and optical fiber temperature sensors, face challenges related to in-situ, real-time temperature monitoring. The proposed in-situ sensor demonstrates distinguished durability for high-temperature monitoring without encapsulations. Leveraging the precise patterning capability of laser writing, the film sensor can be tailored into elaborate patterns suitable for surfaces of diverse components (Figures 5(b) and S24). Assessing the reliability of the sensor is imperative, especially in scenarios requiring repetitive or prolonged exposure to varying temperatures. The temperature sensor maintains superior stability in the temperature monitoring for bearing over a range of 156−800 °C (Figure 5(c)). After 4 cycles (>30 hours), the drift of resistance is only 4.51% at 156 °C and 3.32% at 800 °C, respectively. When converted to temperature, these values correspond to insignificant drifts of 0.97% (1.5 °C) at 156 °C and 0.25% (2 °C) at 800 °C, respectively. This sensor is capable of monitoring bearing temperature across various ranges, even at sub-zero conditions down to −50 °C (Figure 5(d)).

To showcase its response to thermal shock, the sensor is subjected to intermittent flame shocks using a blowtorch. The results reveal that the sensor responds quickly and accurately to transient, different intensities and high-frequency thermal shocks (Figure 5(e)). Furthermore, the friction and vibration that the bearing may experience during operation are evaluated (Figure 5(f)). A piece of sandpaper is placed on the sensor with a press force of 20 N via a compression machine, then moved in a fixed direction repeatedly for 10 cycles to mimic potential wear. Subsequently, the bearing is mounted on a shaft and rotated to simulate the vibrations. During these processes, the robustness of the sensor is evaluated by real-time monitoring of the resistance drift (0.5%, corresponding to ∼0.37 °C). Additionally, the sensor also presents exceptional stability for temperature detection in lubricating oil (Figure S25). Overall, these systematic tests imply that the sensor, fabricated via the proposed method, is a promising candidate for monitoring the temperature of key apparatus in extreme environments, with applicable scenarios including aero-bearing, turbine blades, and engines.

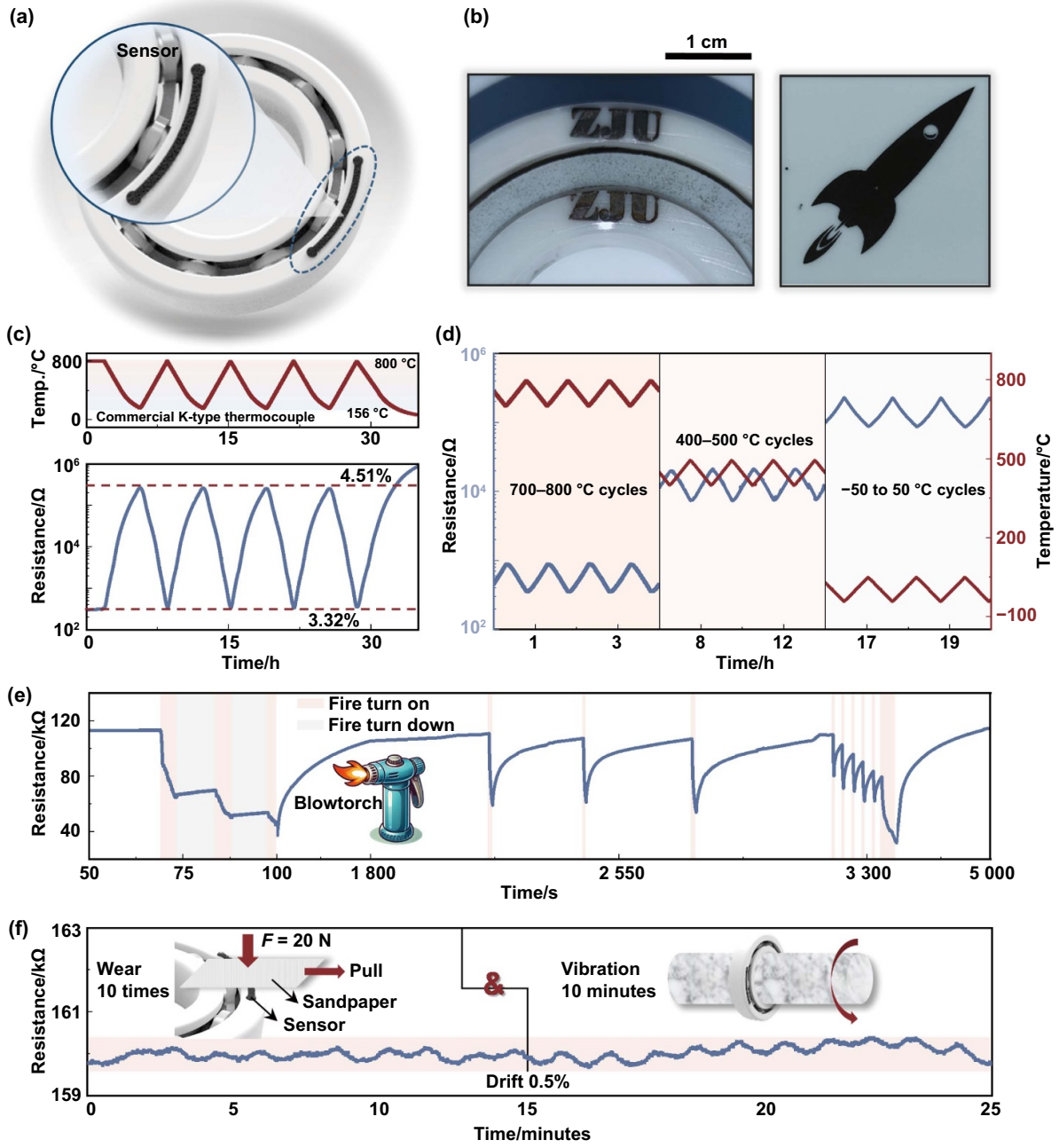

Figure 5. Demonstration of the film-based temperature sensor on ceramic bearing. (a) Schematic of the film-based temperature sensor fabricated on a bearing. (b) Photos of patterned active films on a Si_3N_4 bearing (left) and an Al_2O_3 ceramic (right). (c) Long-time cyclic measurements of the integrated monitoring system compared with a commercial K-type thermocouple under temperature variation from 156 °C to 800 °C. (d) Real-time monitoring of bearing temperature across various temperature ranges (i.e. −50 °C to 50 °C, 400 °C to 500 °C, 700 °C to 800 °C). (e) Response of the temperature sensor under flame shocks of varying intensities and frequencies by a blowtorch. (f) Resistance changes of the temperature sensor after surface abrasion with a sandpaper and under vibrations caused by bearing rotation.

3. Conclusion

This work presents a conductive passivation approach for the realization of an in-situ film temperature sensor on ceramic components. Through physical and chemical processes, instantaneous laser-induced localized thermal effect not only transforms electrically insulated TiB_2/SiC composite inks into conductive and thermal-sensitive TiB_2 traces, but also passivates SiO_2-B_2O_3 layers against oxidation at high temperatures. Such interior crystalline conductive layers and exterior amorphous antioxidative layers are systematically verified by various characterizations. The prototypes fabricated on Al_2O_3 ceramic and Si_3N_4 bearings achieve high-precision temperature monitoring across a wide range from −50 °C to 950 °C, showing a variance of 0.989 5 when fitted to the Steinhart-Hart model. During over 30-hour cycle test, the temperature sensor displays an almost negligible drift of 0.97% (i.e. 1.5 °C) at 156 °C and 0.25% (i.e. 2 °C) at 800 °C.

This work affords a facile yet reliable strategy to fabricate in-situ thin-film-based temperature sensors without extra anti-oxidative encapsulations. Future prospects include the integration of other sensing parameters, such as pressure, strain, and heat shock and the development of high-quality conformal films on varying curved surfaces.

4. Methods

4.1. Preparation of functional TiB_2/SiC ink

The proposed functional TiB_2/SiC ink for the formation of temperature sensor consisted of titanium diboride (TiB_2), silicon carbide (SiC), polyvinyl pyrrolidone (PVP), and isopropyl alcohol (IPA). To prepare this functional ink, 0.446 g of PVP (Mw = 10 000, Aladdin, China) was first dissolved in 5 mL of IPA (>99.7%, General-reagent, China) using a magnetic stirring heater at 60 °C with 1 000 rpm for 1 hour. Then, 3 g of TiB_2 (99%, 1−3 μm, Adamas, China) and 0.6 g SiC (99%, 0.5−0.7 μm, Aladdin, China) were added and ultrasonicated until completely dispersed. The inks of control group were composed of PVP, IPA, and different mass ratios of TiB_2 and SiC. TiB_2 and SiC with various mass ratios were added into the as-prepared solvent and ultrasonicated until uniformly dispersed. The aforementioned chemicals were purchased from shiyangu (www.labgle.com).

4.2. Fabrication of the film-based temperature sensor by laser direct writing

First, a 2 mm-thick α-Al_2O_3 (Jingwei Special Ceramics Co., Ltd, China) substrate was cleaned with isopropanol. Then, 1.5 mL of the as-prepared TiB_2/SiC ink and control groups' inks were dropped onto the α-Al_2O_3 surface, followed by the spin-coating at 500 rpm for 15 seconds. The film can also form through doctor-blading coating and dispensing. Subsequently, the as-prepared ink films were dried for 5 minutes inside an oven at around 60 °C. Then, the resulting ink films were photothermally converted to temperature-sensitive films by applying a CW visible green laser with an energy density between 2 J·mm^{-2} and 10 J·mm^{-2}, a scanning speed of 20 mm·s^{-1}, and a hatch spacing of 20 μm, respectively. The patterned resolution is approximately 64 μm and the depth of focus is approximately 50 μm. The electrical and surface morphological properties of films were flexibly controlled by the processing laser power, hatch spacing as well as the relative contents of compositions in inks. Finally, the temperature-sensitive films were bonded to the platinum (Pt) wires with silver/palladium (Ag/Pd) paste (Shenzhen Sryeo Electronic Paste Co., Ltd., China) to extract the signals.

The fabrication of the monitoring system on bearing was similar to the aforementioned processes. 1.5 mL ink was dropped onto the side of a Si_3N_4 bearing, and spin-coated at 500 rpm for 15 seconds. After the obtained ink films were dried, the films were photothermally converted to temperature-sensitive films by applying a CW visible laser. Finally, the electrical signals were extracted through Pt wires.

4.3. Material characterizations

The surface morphologies of films fabricated by different laser energy densities were captured by an optical microscope (MCK-6RC, Caikon, China). Scanning electron microscopy (SEM) images were acquired at 15 kV by using a ZEISS Sigma 300 to characterize the surface morphologies and elements of the films fabricated by different laser energy densities before and after the durability test. X-ray diffraction (XRD) was performed on a Rigaku SmartLab SE X-ray diffractometer equipped with Copper Kα radiation. Raman spectra were acquired using HORIBA's Raman system with a 532 nm excitation laser (Jobin Yvon S.A.S, France). X-ray photoelectron spectroscopy (XPS) was conducted using a Thermo Scientific K-Alpha to characterize the types of chemical bonds. Transmission electron microscopy (TEM) images and energy dispersive spectroscopy (EDS) images were obtained using a JEOL JEM-F200 field emission transmission electron microscope. TEM samples were prepared by focused ion beam (FIB) using Thermo Fisher Helios G4 UX. FT-IR spectra were acquired by Thermo Fisher Scientific Nicolet iS20. Shiyanjia Lab aided with FT-IR spectra (www.shiyanjia.com).

4.4. Characterizations of electrical properties of films and temperature response

Electrical conductivities and square resistance were tested by an HPS 2662 four-probe test instrument. A home-made calibration system, composed of a tube furnace (Hefei Kejing Materials Technology Co., Ltd., China), a K-type thermocouple, a multi-channel multimeter (DAQ970A & DAQM901A, Keysight, USA), and a computer, was applied to test the performance of the proposed temperature sensor at different temperatures. Due to the limitations of the laboratory environment and instruments, high-temperature tests were all limited to within 50 hours. The low-temperature (−50 °C to 50 °C) cycle tests were carried out using a humidity oven (SH-262, Espec, Japan). The stripping experiment was performed with 3 M tape. The tape stripping test follows the 90° stripping principle. The further adhesion test was conducted by an ultrasonic cleaning machine. The responses of the sensor to convective heat transfer and thermal shock were investigated via instantaneous heating by a flame burner. The wear resistance test was performed by rubbing the surface of the film with sandpaper, which was pressed against the film by a compression force of 20 N. The vibration of anti-vibration test was applied by bearing rotation.

Acknowledgments

The authors acknowledge the financial support from the National Natural Science Foundation of China (52475610, 52105593), the Zhejiang Provincial Natural Science Foundation of China (LDQ24E050001), the "Pioneer" and "Leading Goose" R&D Program of Zhejiang (2023C03007, 2024C01173), and the Fundamental Research Funds for the Central Universities (226-2024-00085). The authors thank the

valuable discussions with Prof. Zhenyin Hai from Xiamen University.

Contributions

Y. H., K. X., and H. X. conceived the idea and designed the research. Y. H. and K. X. wrote the manuscript. K. X., H. X., and H. Y. supervised the project. Y. H. prepared the samples, fabricated the device, performed the experiments, as well as conducted the characterizations. Y. L. and Z. C. provided extensive suggestions on experimental design. Y. J. and B. Z. provided valuable guidance on the material characterizations. All the authors discussed the results and commented on the manuscript.

References

[1] Li G R et al. 2021. Self-powered soft robot in the Mariana Trench. *Nature* **591**, 66–71.
[2] Zhao K, Zhang T F, Chang H C, Yang Y, Xiao P S, Zhang H T, Li C X, Tiwary C S, Ajayan P M and Chen Y S. 2019. Super-elasticity of three-dimensionally cross-linked graphene materials all the way to deep cryogenic temperatures. *Sci. Adv.* **5**, eaav2589.
[3] Wyatt B C, Nemani S K, Hilmas G E, Opila E J and Anasori B. 2024. Ultra-high temperature ceramics for extreme environments. *Nat. Rev. Mater.* **9**, 773–789.
[4] Lu Y Y et al. 2023. Stretchable graphene-hydrogel interfaces for wearable and implantable bioelectronics. *Nat. Electron.* **7**, 51–65.
[5] Huang X H, Liu L S, Lin Y H, Feng R, Shen Y Y, Chang Y N and Zhao H B. 2023. High-stretchability and low-hysteresis strain sensors using origami-inspired 3D mesostructures. *Sci. Adv.* **9**, eadh9799.
[6] Yang L, Chen X, Dutta A, Zhang H, Wang Z H, Xin M Y, Du S J, Xu G Z and Cheng H Y. 2025. Thermoelectric porous laser-induced graphene-based strain-temperature decoupling and self-powered sensing. *Nat. Commun.* **16**, 792.
[7] Ni D W et al. 2022. Advances in ultra-high temperature ceramics, composites, and coatings. *J. Adv. Ceram.* **11**, 1–56.
[8] Oses C, Toher C and Curtarolo S. 2020. High-entropy ceramics. *Nat. Rev. Mater.* **5**, 295–309.
[9] Liu Y H et al. 2025. Triboelectric tactile sensor for pressure and temperature sensing in high-temperature applications. *Nat. Commun.* **16**, 383.
[10] Xu K C, Cai Z M, Luo H Y, Lin X Y, Yang G, Xie H B, Ko S H and Yang H Y. 2024. An *in-situ* hybrid laser-induced integrated sensor system with antioxidative copper. *Int. J. Extrem. Manuf.* **6**, 065501.
[11] Liu Z J, Tian B, Jiang Z D, Li S M, Lei J M, Zhang Z K, Liu J J, Shi P and Lin Q J. 2023. Flexible temperature sensor with high sensitivity ranging from liquid nitrogen temperature to 1200 °C. *Int. J. Extrem. Manuf.* **5**, 015601.
[12] Shin J et al. 2020. Sensitive wearable temperature sensor with seamless monolithic integration. *Adv. Mater.* **32**, 1905527.
[13] Yu H L, Hu Z Q, He J, Ran Y J, Zhao Y, Yu Z and Tai K P. 2024. Flexible temperature-pressure dual sensor based on 3D spiral thermoelectric Bi_2Te_3 films. *Nat. Commun.* **15**, 2521.
[14] Wang J L, Liu Y, Liu T, Zhang S, Wei Z, Luo B, Cai C, Chi M, Wang S and Nie S. 2024. Dynamic thermostable cellulosic triboelectric materials from multilevel-non-covalent interactions. *Small* **20**, 2307504.
[15] Li X J, Zhang L, Feng Y, Zheng Y, Wu Z, Zhang X, Wang N, Wang D and Zhou F. 2021. Reversible temperature-sensitive liquid–solid triboelectrification with polycaprolactone material for wetting monitoring and temperature sensing. *Adv. Funct. Mater.* **31**, 2010220.
[16] Thuruthel T G, Shih B, Laschi C and Tolley M T. 2019. Soft robot perception using embedded soft sensors and recurrent neural networks. *Sci. Robot.* **4**, eaav1488.
[17] Wei Z B, Hu J, He H W, Yu Y F and Marco J. 2023. Embedded distributed temperature sensing enabled multistate joint observation of smart lithium-ion battery. *IEEE Trans. Ind. Electron.* **70**, 555–565.
[18] Chen G C et al. 2023. Conformal fabrication of functional polymer-derived ceramics thin films. *Surf. Coat. Technol.* **464**, 129536.
[19] Yu J C, Hu C X, Wang Z, Wei Y K, Liu Z J, Li Q G, Zhang L, Tan Q L and Zang X N. 2023. Printing three-dimensional refractory metal patterns in ambient air: toward high temperature sensors. *Adv. Sci.* **10**, 2302479.
[20] Chen X Y et al. 2023. Wrap-like transfer printing for three-dimensional curvy electronics. *Sci. Adv.* **9**, eadi0357.
[21] Chen Z Y, Wang Y Z, Huang Y L, Peng F, Lin C C, Zheng W, Song X M, Niu Y R and Zeng Y. 2024. Investigation on improving the comprehensive performance of environmental barrier coating materials by high-entropy multiphase design. *npj Mater. Degrad.* **8**, 37.
[22] Padture N P. 2016. Advanced structural ceramics in aerospace propulsion. *Nat. Mater.* **15**, 804–809.
[23] Wei Z Y et al. 2022. Progress in ceramic materials and structure design toward advanced thermal barrier coatings. *J. Adv. Ceram.* **11**, 985–1068.
[24] Wu Q L, Long W M, Zhang L and Zhao H W. 2024. A review on ceramic coatings prepared by laser cladding technology. *Opt. Laser Technol.* **176**, 110993.
[25] Chen L, Li B H, Guo J, Zhu Y K and Feng J. 2022. High-entropy perovskite $RETa_3O_9$ ceramics for high-temperature environmental/thermal barrier coatings. *J. Adv. Ceram.* **11**, 556–569.
[26] Zhang X F et al. 2020. Al_2O_3-modified PS-PVD 7YSZ thermal barrier coatings for advanced gas-turbine engines. *npj Mater. Degrad.* **4**, 31.
[27] Sheng A, Khuje S, Yu J, Petit D, Parker T, Zhuang C G, Kester L and Ren S Q. 2021. Ultrahigh temperature copper-ceramic flexible hybrid electronics. *Nano Lett.* **21**, 9279–9284.
[28] Zeng Y J et al. 2023. Metal-based sandwich type thick-film platinum resistance temperature detector for in-situ temperature monitoring of hot-end components. *Appl. Surf. Sci.* **637**, 157979.
[29] Hai Z Y, Guo M C, Xu L D, Su Z X, Wang Y S, He Y P, Zhao Y and Sun D H. 2024. Printable silicate and RuO_2 composite with wide-range linear PTC for high-temperature sensors. *Ceram. Int.* **50**, 30776–30784.
[30] Chaudhary R P, Parameswaran C, Idrees M, Rasaki A S, Liu C Y, Chen Z W and Colombo P. 2022. Additive manufacturing of polymer-derived ceramics: materials, technologies, properties and potential applications. *Prog. Mater. Sci.* **128**, 100969.
[31] Meng B, Wang J L, Chen M H, Zhu S L and Wang F H. 2023. Study on the oxidation behavior of a novel thermal barrier coating system using the nanocrystalline coating as bonding coating on the single-crystal superalloy. *Corros. Sci.* **225**, 111591.
[32] Yin C, Zhang T, Zhang C, Zhang Y, Jeong C K, Hwang G-T and Chi Q. 2024. Flexible mica films coated by magnetron sputtered insulating layers for high-temperature capacitive energy storage. *SusMat* **4**, e228.
[33] Hu P, Hu P, Vu T D, Li M, Wang S, Ke Y, Zeng X, Mai L and Long Y. 2023. Vanadium oxide: phase diagrams, structures, synthesis, and applications. *Chem. Rev.* **123**, 4353–4415.

[34] Shepelin N A, Tehrani Z P, Ohannessian N, Schneider C W, Pergolesi D and Lippert T. 2023. A practical guide to pulsed laser deposition. *Chem. Soc. Rev.* **52**, 2294–2321.
[35] Choo S, Varshney S, Liu H, Sharma S, James R D and Jalan B. 2024. From oxide epitaxy to freestanding membranes: opportunities and challenges. *Sci. Adv.* **10**, eadq8561.
[36] Kong M et al. 2024. Ambient printing of native oxides for ultrathin transparent flexible circuit boards. *Science* **385**, 731–737.
[37] Shan Y, Liu S Y, Wang B, Hong Y, Zhang C, Lim C W, Zhang G Z and Yang Z B. 2021. A gravity-driven sintering method to fabricate geometrically complex compact piezoceramics. *Nat. Commun.* **12**, 6066.
[38] Deng B, Eddy L, Wyss K M, Tiwary C S and Tour J M. 2025. Flash Joule heating for synthesis, upcycling and remediation. *Nat. Rev. Clean Technol.* **1**, 32–54.
[39] Zhou C C, Liang S S, Qi B, Liu C X and Cho N J. 2024. One-pot microfluidic fabrication of micro ceramic particles. *Nat. Commun.* **15**, 8862.
[40] Hordieiev Y S, Karasik E V and Zaichuk A V. 2023. Glass formation in the $MgO–B_2O_3–SiO_2$ system. *Silicon* **15**, 1085–1091.
[41] Al-Baradi A M, Wahab E A A and Shaaban K S. 2022. Preparation and characteristics of B_2O_3—SiO_2—Bi_2O_3—TiO_2—Y_2O_3 glasses and glass-ceramics. *Silicon* **14**, 5277–5287.
[42] Rockett T J and Foster W R. 1965. Phase relations in the system boron oxide–silica. *J. Am. Ceram. Soc.* **48**, 75–80.
[43] Wuchina E, Opila E, Opeka M, Fahrenholtz B and Talmy I. 2007. UHTCs: ultra-high temperature ceramic materials for extreme environment applications. *Electrochem. Soc. Interface* **16**, 30.
[44] Shur M, Rumyantsev S and Levinshtein M. 2006. *SiC Materials and Devices*. (World Scientific, Singapore).
[45] Adrievskii R A. 1994. Properties of nanocrystalline refractory compounds. *Powder Metall. Met. Ceram.* **32**, 935–941.
[46] Wdowik U D, Twardowska A and Rajchel B. 2017. Vibrational spectroscopy of binary titanium borides: first-principles and experimental studies. *Adv. Condens. Matter Phys.* **2017**, 4207301.
[47] Challagulla S, Tarafder K, Ganesan R and Roy S. 2017. Structure sensitive photocatalytic reduction of nitroarenes over TiO_2. *Sci. Rep.* **7**, 8783.
[48] McKeown D A, Muller I S, Buechele A C, Pegg I L and Kendziora C A. 2000. Structural characterization of high-zirconia borosilicate glasses using Raman spectroscopy. *J. Non-Cryst. Solids* **262**, 126–134.
[49] Greer A L. 1995. Metallic glasses. *Science* **267**, 1947–1953.
[50] Lu Z P and Liu C T. 2003. Glass formation criterion for various glass-forming systems. *Phys. Rev. Lett.* **91**, 115505.
[51] Steinhart J S and Hart S R. 1968. Calibration curves for thermistors. *Deep Sea Res. Oceanogr. Abstr.* **15**, 497–503.